



Article

# Strong Linear Correlation between CH<sub>3</sub>NH<sub>2</sub> Molecular Defect and THz-Wave Absorption in CH<sub>3</sub>NH<sub>3</sub>PbI<sub>3</sub> Hybrid Perovskite Thin Film

Inhee Maeng <sup>1,†</sup>, Asuka Matsuyama <sup>2</sup>, Jung-Ho Yun <sup>3</sup>, Shenghao Wang <sup>4</sup>, Chul Kang <sup>1</sup>, Chul-Sik Kee <sup>1</sup>, Masakazu Nakamura <sup>2</sup> and Min-Cherl Jung <sup>5,\*</sup>

<sup>1</sup> Advanced Photonics Research Institute, Gwangju Institute of Science and Technology, Gwangju 61005, Korea; inheem@yuhs.ac (I.M.); iron74@gist.ac.kr (C.K.); cskee@gist.ac.kr (C.-S.K.)

<sup>2</sup> Division of Materials Science, Nara Institute of Science and Technology, Nara 630-0192, Japan; matsuyama.asuka.lr5@ms.naist.jp (A.M.); mnakamura@ms.naist.jp (M.N.)

<sup>3</sup> School of Chemical Engineering and Australian Institute for Bioengineering and Nanotechnology (AIBN), University of Queensland, Brisbane QLD 4027, Australia; j.yun1@uq.edu.au

<sup>4</sup> Materials Genome Institute, Shanghai University, Shanghai 200444, China; shenghaowang@shu.edu.cn or shenghao.wang@oist.jp

<sup>5</sup> Division of Materials Science, Faculty of Pure and Applied Sciences, University of Tsukuba, Ibaraki 305-8577, Japan

\* Correspondence: jung.mincherl.fp@u.tsukuba.ac.kr; Tel.: +81-29-853-4995

† Current affiliation: YUHS-KRIBB, Medical Convergence Research Institute, College of Medicine, Yonsei University, Seoul 03722, Korea.

Received: 11 March 2020; Accepted: 7 April 2020; Published: 10 April 2020



**Abstract:** To control the density of a CH<sub>3</sub>NH<sub>2</sub> molecular defect, which strongly contributed to a significant THz-wave absorption property in the CH<sub>3</sub>NH<sub>3</sub>PbI<sub>3</sub> hybrid perovskite thin film formed by the sequential vacuum evaporation method, we performed post-annealing processes with various temperatures and times. In the thin film after post-annealing at 110 °C for 45 min, the density of the CH<sub>3</sub>NH<sub>2</sub> molecular defect was minimized, and CH<sub>3</sub>NH<sub>3</sub>I and PbI<sub>2</sub> disappeared in the thin film after the post-annealing process at 150 °C for 30 min. However, the density of the CH<sub>3</sub>NH<sub>2</sub> molecular defect increased. Moreover, the THz-wave absorption property for each thin film was obtained using a THz time-domain spectroscopy to understand the correlation between the density of a molecular defect and the THz-wave oscillation strength at 1.6 THz, which originated in the molecular defect-incorporated hybrid perovskite structure. There is a strong linear correlation between the oscillator strength of a significant THz-wave absorption at 1.6 THz and the CH<sub>3</sub>NH<sub>2</sub> molecular defect density.

**Keywords:** CH<sub>3</sub>NH<sub>2</sub>; THz oscillation strength; MAPbI<sub>3</sub>

## 1. Introduction

Recently, the organic–inorganic hybrid perovskite (OHP) material ABX<sub>3</sub> (A = Organic cation: CH<sub>3</sub>NH<sub>3</sub><sup>+</sup>/NH<sub>2</sub>CH=NH<sub>2</sub><sup>+</sup>, B = Metal cation: Pb/Sn, and X = Halide anion: Cl/Br/I) has been identified as a potential application material for solar cell, field-effect transistor, and light-emitting diode applications [1–7]. In the last decade, many works have been reported in OHP material research [8]. Even nano-scaled formation research using OHP material has just begun, and its single crystal formation with nano-size and physical properties, such as bandgap engineering, have been reported [9–11]. New applications employing these OHP materials are expected to be further expanded, due to several unique physical properties that are still unclear. In our previous research, we found several significant

THz-wave absorptions in  $\text{CH}_3\text{NH}_3\text{PbI}_3$  (MAPbI<sub>3</sub>) and  $\text{HC}(\text{NH}_2)_2\text{PbI}_3$  (FAPbI<sub>3</sub>) that originated in a kind of defect structure [12–14]. Particularly, we found that the origin of absorptance in MAPbI<sub>3</sub> was the  $\text{CH}_3\text{NH}_2$  molecular defect-incorporated perovskite structure (significant I–Pb–I vibration mode) [13]. This finding shows an interesting possibility for a new application, such as THz-wave modulation, sensing, and imaging devices instead of high purified GaAs formed at low temperature with an expensive unit price and ultra-high vacuum-based fabrication [15,16]. This means that we need to find and improve on a controllable physical property, such as the strength control of an I–Pb–I vibration mode.

However, another problem arises, such as the material stability because there is no post-annealing process to keep the presence of a molecular defect [13,14,17–19]. Generally, the post-annealing process can induce more stable OHP with large grains and clear stoichiometry. On the other hand, we can guess easily that the neutral molecular defect such as  $\text{CH}_3\text{NH}_2$  will disappear during post-annealing. In short, it is required to find an optimized condition to (1) ensure material stability in the OHP thin film and (2) maintain enough density of the  $\text{CH}_3\text{NH}_2$  molecular defect for the significant vibration mode.

In this article, MAPbI<sub>3</sub> thin films fabricated with the sequential vacuum evaporation (SVE) method [12,13,20,21] are performed using the post-annealing process with various temperatures and times. We then investigate their atomic structures, defects, and chemical states to find an optimized state with the control of defect density and the improvement of stability. Finally, we look for a linear correlation between the density of  $\text{CH}_3\text{NH}_2$  molecular defect and the THz-wave oscillator strength to lead to the key possibility of new applications, such as THz-wave modulation, sensing, and imaging devices.

## 2. Materials and Methods

OHP thin films were fabricated using the SVE method in the customized vacuum chamber [13,21]. A silicon substrate (*n*-type doped Si(100)) was cleaned by sonication in acetone for 10 min and then rinsed in heated acetone for 1 min. After this, a UV-ozone treatment was performed for 30 min before loading it into a vacuum chamber. In addition, the  $\text{Al}_2\text{O}_3$  substrates (made by Hi-Solar Co., Ltd., Gwangju, Korea) were used for the measurement of THz time-domain spectroscopy (THz-TDS). The surface orientation is C-plane(0001) with an off-angle of  $0.2^\circ \pm 0.05^\circ$ . The thickness and roughness are  $430 \pm 25 \mu\text{m}$  and  $R_a \leq 0.3 \text{ nm}$ , respectively. The cleaning method is the same. The base pressure of the chamber installed with the thickness monitor sensor was  $8.0 \times 10^{-3} \text{ Pa}$ . A Lead(II) iodide ( $\text{PbI}_2$ , 99% purity, Sigma-Aldrich, St. Louis, MO, USA) was evaporated with a deposition rate of  $10 \text{ \AA/s}$  onto the substrates at room temperature to form the film with a 100 nm thickness (Figure 1). Continuously, a methylammonium iodide ( $\text{CH}_3\text{NH}_3\text{I}$ , 98% purity, Sigma-Aldrich, St. Louis, MO, USA) was evaporated with a deposition rate of  $2 \text{ \AA/s}$  and a 280 nm thickness onto the formed  $\text{PbI}_2$  thin film. Finally, we obtained the MAPbI<sub>3</sub> thin films with a thickness of 300 nm [21] (Figure 1). To see the temperature dependence of MAPbI<sub>3</sub>, we performed the annealing processes at a temperature of 110 °C for 45 min (the typical annealing condition for solar cell application) and 150 °C for 10 and 30 min (to avoid any dramatical material degradation) [21]. Over a temperature of 150 °C, the depletion/degradation processes of MAPbI<sub>3</sub> were so fast that it was very difficult to maintain a hybrid perovskite structure. To characterize all of the formed and treated thin films, we performed scanning electron microscopy (SEM), X-ray diffraction (XRD), and high-resolution X-ray photoelectron spectroscopy (XPS). The used SEM system is the HITACHI SU9000 model (Tokyo, Japan) with an acceleration voltage of 5.0 kV and an emission current of 10  $\mu\text{A}$ . The model of XRD with a  $\text{CuK}_\alpha$  source is RINT-TTRIII/NM made by Rigaku (Tokyo, Japan). We used the VersaProbe II (Chigasaki, Japan) with a monochromated  $\text{AlK}_\alpha$  (ULVAC-PHI, (Chigasaki, Japan) for all XPS measurements and obtained the C 1s, N 1s, Pb 4f, and I 4d core-level spectra. In all samples, no traces of  $\text{O}_{1s}$  core-level spectra were observed. The binding energies were calibrated with reference to the Au 4f<sub>7/2</sub> level (84.0 eV) [22]. The THz spectra were measured with a standard THz-TDS transmission setup based on a Ti:Sapphire regenerative amplifier system, which has 35 fs pulses at an 800 nm wavelength and a repetition rate

of 1 kHz. We used a 2 mm ZnTe(110) crystal for generation and detection. We measured the THz time-domain signal in the spectral range from 0.5 up to 2.5 THz. We measured the THz-TDS spectra of the formed and treated thin films on the  $\text{Al}_2\text{O}_3$  substrate, and the THz conductivity was obtained from a thin film approximation equation [23].

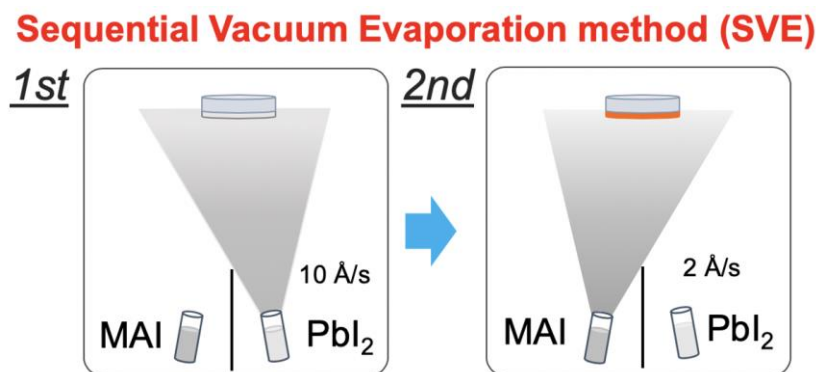


Figure 1. The schematic of the sequential vacuum evaporation (SVE) method.

### 3. Results and Discussion

In the no-annealed sample (A), we can observe a tiny grain structure (Figure 2a). However, its grain boundary is not clear. After annealing at 110 °C for 45 min (B), which is a typical annealing condition for a solution-processed thin film in solar cell application, the grains appear clearly with a grain size of 70–120 nm (Figure 2b). While increasing the annealing temperature at 150 °C for 10 min, the grain size increased over 200 nm (Figure 2c). By increasing the annealing time for 30 min at 150 °C, however, many small structures occurred at the grain boundary, and it looks like a surface degradation (Figure 2d). From these SEM results, we can agree that (1) the annealing process with a high temperature can increase the grain size, and (2) the increased annealing time can cause a degradation at the grain boundary [13,14,20,21].

To understand the structural formation, we performed the XRD experiment for all treated samples (Figure 2e). In all samples, the typical atomic structures of  $\text{MAPbI}_3$  were observed, such as (110), (112), (202), (220), (222), (204), and (312) in the range of 5–40° [21]. In the A sample, we can observe the trace of  $\text{CH}_3\text{NH}_3\text{I}$  (MAI),  $\text{PbI}_2$ , and intermediate phases (the  $\text{CH}_3\text{NH}_2$  incorporated hybrid perovskite structure) [21]. In the B sample, however, these structures have completely disappeared. We confirmed that the typical annealing condition for a solar cell application could remove the MAI and  $\text{PbI}_2$  phases formed by the SVE method [13,21]. When we increased the annealing temperature from 100 to 150 °C (the sample C), the MAI,  $\text{PbI}_2$ , and the intermediate phases were still alive. When increasing the annealing time from 10 to 30 min at 150 °C (the D sample), only the intermediate phase, which originated in the  $\text{CH}_3\text{NH}_2$  molecular defect-incorporated perovskite structure, has remained mainly with the hybrid perovskite phase, and the MAI and  $\text{PbI}_2$  phases have wholly disappeared [21].

To see changes of chemical states in all treated samples, we performed a high-resolution XPS experiment. The C 1s, N 1s, Pb 4f, and I 4d core-level spectra were obtained for each sample (Figure 3). First of all, we can notice that the chemical states of N 1s (402.7 eV at the maximum intensity peak position) and I 4d ( $I 4d_{5/2} = 619.5$  eV) almost did not change on any annealing conditions [13,21] (Figure 3b,d). The A sample was observed consistently with our previous reports [20]. The typical chemical states of  $\text{CH}_3\text{NH}_3^+$  cation (C 1s—287.0 eV and N 1s—402.7 eV) and the  $\text{CH}_3\text{NH}_2$  molecular defect (C 1s—286.0 eV and N 1s—403.3 eV) were observed in the C 1s and N 1s core-level spectra [13,21] (Figure 3a,b). The peak intensity of the  $\text{CH}_3\text{NH}_2$  molecular defect decreased after annealing, and the  $\text{Pb}^{0+}$  chemical state (Pb metal) appeared at the 150 °C annealing temperature [13,21] (Figure 3a,c). This means that the hybrid perovskite structure on the surface was broken at the high-temperature

annealing process. Moreover, the molecular defect and I-related elements were depleted from the surface, and only the Pb metal element remained on the surface.

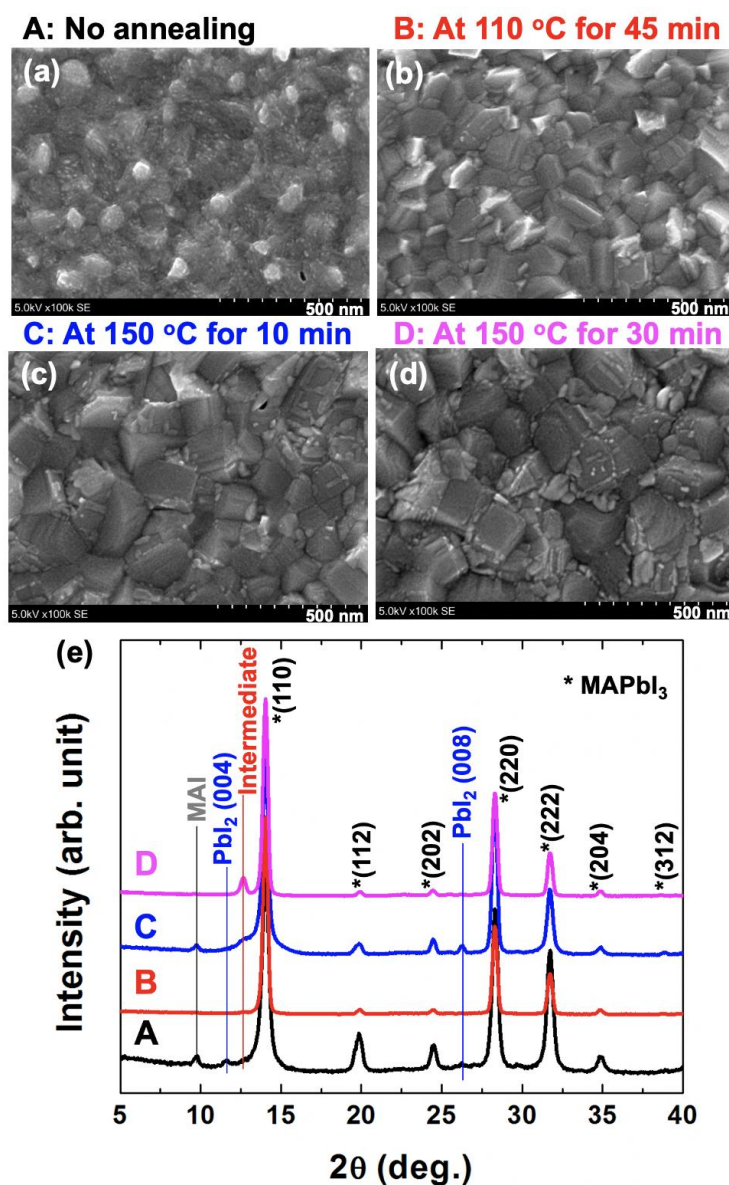


**Figure 2.** (a–d) The surface morphologies by SEM measurements and (e) XRD results with variable post-annealing conditions, A: No annealing, B: At 110 °C for 45 min, C: At 150 °C for 10 min, and D: At 150 °C for 30 min. In the typical annealing condition (B: for solar cell application) for MAPbI<sub>3</sub> (\*), MAI, PbI<sub>2</sub>, and intermediate phases were not observed.

To see the detailed behavior of the CH<sub>3</sub>NH<sub>2</sub> molecular defect processed under the different annealing conditions, we performed curve fittings of C 1s core-level spectra in samples A, B, C, and D using Doniach–Sünjić curves convoluted with Gaussian distribution with 0.5 eV full width at half maximum [24] (Figure 4a). The background due to inelastic scattering was subtracted via the Shirley (integral) method [25]. Interestingly, we observed a very small defect intensity in the B sample. However, the C and D samples were still shown with the CH<sub>3</sub>NH<sub>2</sub> molecular defect. From the curve-fitting data, we calculated the relative intensity area for each sample (Figure 4b). In the A sample, we confirmed over 18% of the concentration of the CH<sub>3</sub>NH<sub>2</sub> molecular defect. However, the molecular defect had almost disappeared after annealing at 110 °C for 45 min, which is a typical annealing

condition for a solar cell application. Interestingly, the  $\text{CH}_3\text{NH}_2$  molecular defect still remained in the samples C and D annealed at 150 °C for 10 min and 30 min, respectively.

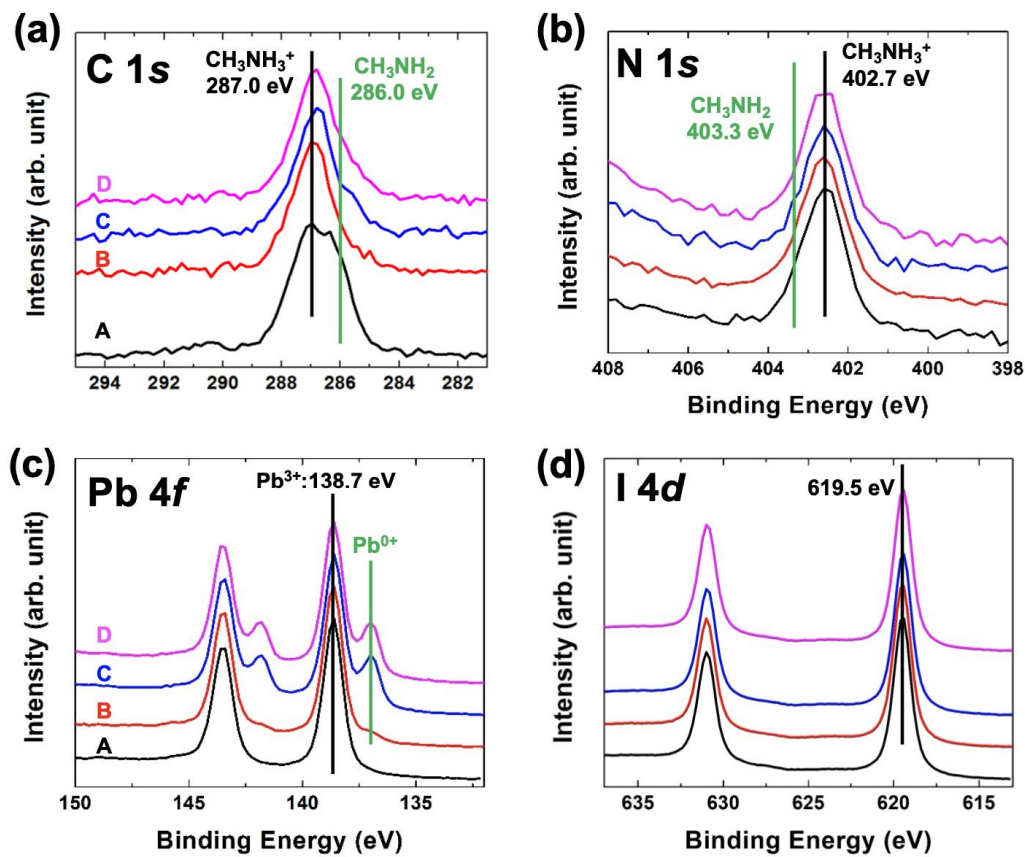


**Figure 3.** (a) C 1s, (b) N 1s, (c) Pb 4f, and (d) I 4d Core-level spectra with A: As received, B: 110 °C/45 min, C: 150 °C/10 min, and D: 150 °C/30 min in  $\text{N}_2$  atmosphere. We observed clearly the chemical states of (1)  $\text{CH}_3\text{NH}_2$  molecular defect and (2)  $\text{Pb}^{0+}$  metal.

The THz real conductivities of all samples show a strong resonance feature, which can be fitted by Lorentzian oscillator model (Equation (1)):

$$\tilde{\varepsilon}(\omega) = \varepsilon_{\infty} + \sum_j \frac{\Omega_j^2}{(\omega_{0j}^2 - \omega^2) - i\gamma_j\omega} \quad (1)$$

where  $\omega_{0j}$ ,  $\Omega_j$ , and  $\gamma_j$ , are resonance frequency, oscillator strength, and the scattering rate of  $j$ th oscillator, respectively [23] (Figure 5a,b). The permittivity constant in the high frequency limit  $\varepsilon_{\infty}$  is not in this experimental spectral range. The spectra are well fitted by three resonance peak frequencies of 1, 1.6, and 2 THz (Table 1). The two peaks around 1 and 2 THz are associated with the Pb–I vibrations of the inorganic components [13,26]. There is no correlation between the oscillator strength ( $\Omega/2\pi$ ) of these peaks and the  $\text{CH}_3\text{NH}_2$  molecular defect. However, in the case of the peak at 1.6 THz, we can clearly observe the correlation between the oscillator strength and the relative intensity area of the  $\text{CH}_3\text{NH}_2$  molecular defect (Figure 5c).

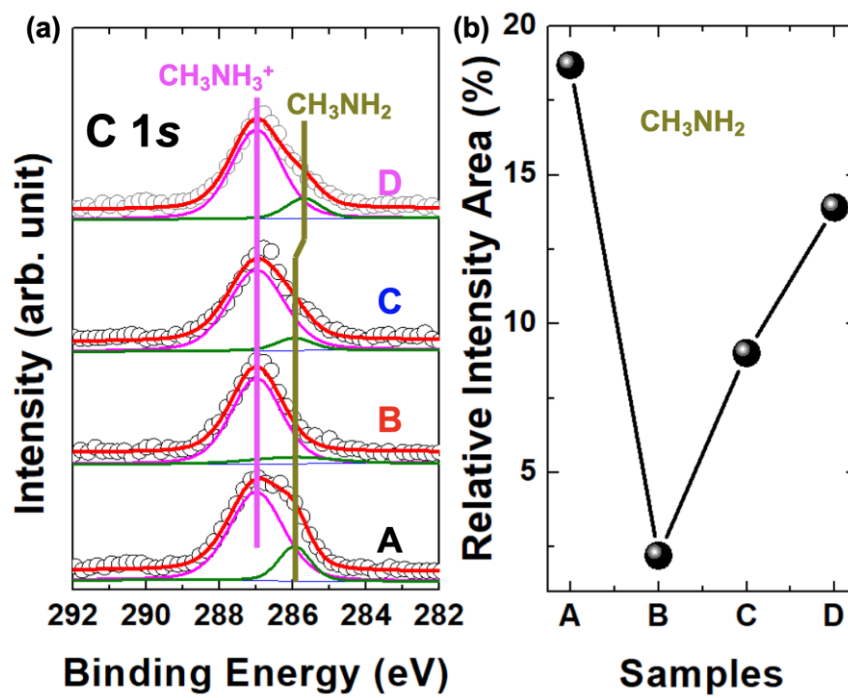


**Figure 4.** (a) Curve fittings for C 1s core-levels of A, B, C, and D. (b) The relative intensity areas for the chemical state of the  $\text{CH}_3\text{NH}_2$  molecular defect.

**Table 1.** The fitting results of collection of Lorentz oscillators.

| Sample | $\omega_0/2\pi$<br>[THz] | $\Omega/2\pi$<br>[THz] | $\gamma/2\pi$<br>[THz] |
|--------|--------------------------|------------------------|------------------------|
| A      | 0.97                     | 3.19                   | 0.389                  |
|        | 1.62                     | 4.29                   | 0.37                   |
|        | 2.03                     | 1.14                   | 0.15                   |
|        | 0.95                     | 2.66                   | 0.272                  |
| B      | 1.62                     | 3.64                   | 0.319                  |
|        | 1.91                     | 3.36                   | 0.395                  |
|        | 0.95                     | 2.51                   | 0.276                  |
| C      | 1.63                     | 3.92                   | 0.274                  |
|        | 1.98                     | 3.88                   | 0.549                  |
|        | 0.96                     | 2.66                   | 0.269                  |
| D      | 1.64                     | 4.03                   | 0.343                  |
|        | 1.9                      | 3.66                   | 0.59                   |

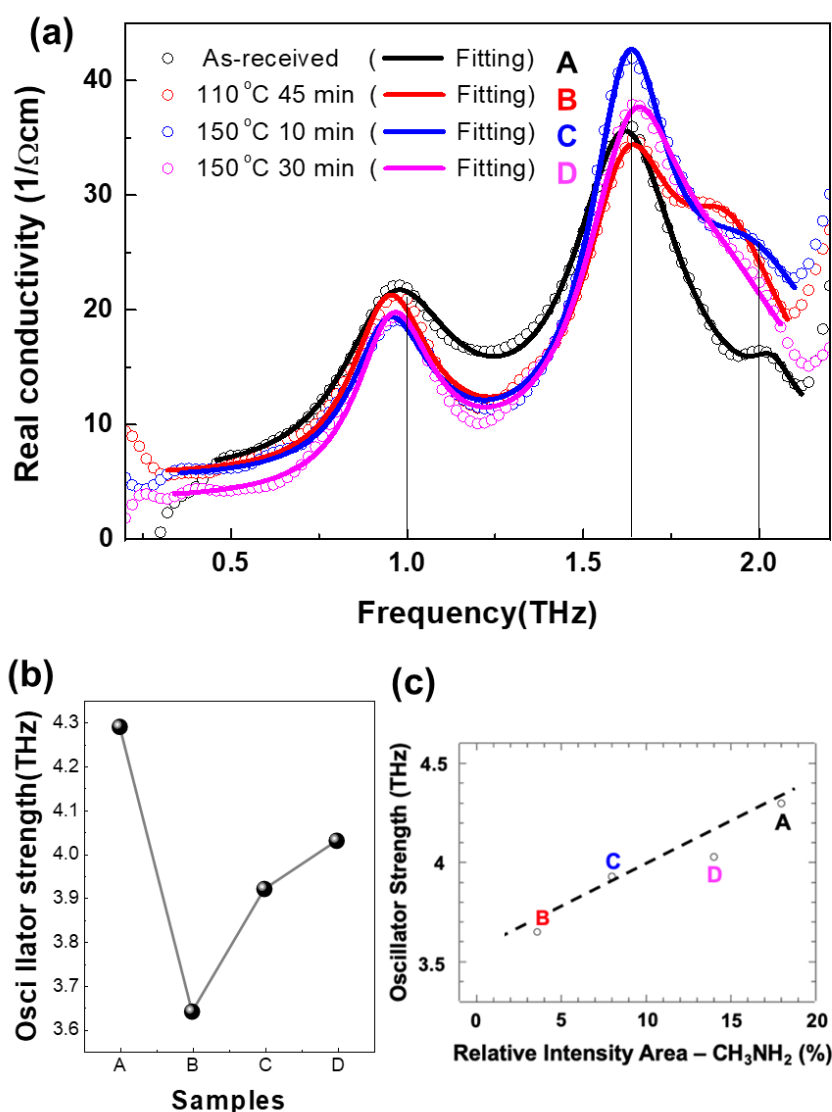


**Figure 5.** (a) THz real conductivities of A, B, C, and D. The Lorentz oscillator model fitting results are plotted by line. (b) The fitting results of oscillator strength of the 1.6 THz resonance peak. (c) The correlation between (b) and the relative intensity area for the chemical state of the  $\text{CH}_3\text{NH}_2$  molecular defect (Figure 3b).

#### 4. Conclusions

In our previous article, we found that the significant THz-wave absorption property originated in the  $\text{CH}_3\text{NH}_2$  molecular defect-incorporated hybrid perovskite [13]. However, the relationship between the strength of THz-wave absorption and the  $\text{CH}_3\text{NH}_2$  molecular defect was not understood quantitatively. It is important to control a THz-wave sensitivity for THz-based applications, such as sensors and modulators. To control the THz-wave oscillator strength in the range of 0.5 to 2.5 THz in a  $\text{MAPbI}_3$  hybrid perovskite thin film, in this article, we needed to control the density of the  $\text{CH}_3\text{NH}_2$  molecular defect, which is controlled by a simple post-annealing process. There is the linear correlation between the defect density and the THz-wave oscillator strength at the 1.6 THz significant absorption in the  $\text{MAPbI}_3$  hybrid perovskite formed by the SVE method. For this to be a new application such as for THz-wave modulation, sensing, and imaging devices, we believe more wide-range and high absorptance properties are needed. For future research, additionally, we suggest an exchange or mixture of metal cation (Pb and Sn) and halogen anion (Cl, Br, and I) elements that will be induced with the different vibration modes in cation and anion structures of the hybrid perovskite structure.

**Author Contributions:** M.-C.J. conceived the idea, designed the experiments, and supervised the project. I.M. and A.M. performed a major portion of the sample preparation and characterization. C.K. and C.-S.K. supported the THz-TDS measurement. J.-H.Y., S.W., and M.N. supported and characterized all the samples. All authors discussed the results, performed data analysis and explanation, wrote the manuscript, and revised it. All authors have read and agreed to the published version of the manuscript.

**Acknowledgments:** This work was supported by funding from JSPS KAKENHI Grant No. 17K05033 (Japan). This work was also supported by the Gwangju Institute of Science and Technology Research Institute (GRI) grant funded by the GIST in 2020 and the Basic Science Research Program (Grant No. NRF2018R1D1A1B07047762) through the National Research Foundation of Korea (NRF), funded by the Ministry of Education in the Republic of Korea. This work was also supported by the Australia Research Council through its DECRA and DP programs. This work was also supported by the Programs for Professor of Special Appointment and Distinguished Visiting Professor (Eastern Scholar) at the Shanghai Institutions of Higher Learning and the Shanghai Rising-Star Program (Grant No. 19QA1403800).

**Conflicts of Interest:** The authors declare no conflict of interest.

## References

1. Service, R.F. Turning up the light. *Science* **2013**, *342*, 794–797. [[CrossRef](#)] [[PubMed](#)]
2. Park, N.G.; Miyasaka, T.; Grätzel, M. *Organic-Inorganic Halide Perovskite Photovoltaics*; Springer: Cham, Switzerland, 2016.
3. Lin, H.; Zhou, C.; Tian, Y.; Siegrist, T.; Ma, B. Low-dimensional organometal halide perovskites. *ACS Energy Lett.* **2017**, *3*, 54–62. [[CrossRef](#)]
4. Loi, M.A.; Hummelen, J.C. Hybrid solar cells: Perovskites under the Sun. *Nat. Mater.* **2013**, *12*, 1087–1089. [[PubMed](#)]
5. Song, T.-B.; Chen, Q.; Zhou, H.; Jiang, C.; Wang, H.-H.; Yang, Y.; Liu, Y.; You, J.; Yang, Y. Perovskite solar cells: Film formation and properties. *J. Mater. Chem. A* **2015**, *3*, 9032–9050. [[CrossRef](#)]
6. Senanayak, S.P.; Yang, B.; Thomas, T.H.; Giesbrecht, N.; Huang, W.; Gann, E.; Nair, B.; Goedel, K.; Guha, S.; Moya, X.; et al. Understanding charge transport in lead iodide perovskite thin-film field-effect transistors. *Sci. Adv.* **2017**, *3*, e1601935. [[CrossRef](#)] [[PubMed](#)]
7. Stranks, S.D.; Snaith, H.J. Metal-halide perovskites for photovoltaic and light-emitting devices. *Nat. Nanotechnol.* **2015**, *10*, 391–402. [[CrossRef](#)]
8. Perovskite Fever. *Nat. Mater.* **2014**, *13*, 837. [[CrossRef](#)]
9. Liu, P.; He, X.; Ren, J.; Liao, Q.; Yao, J.; Fu, H. Organic–inorganic hybrid perovskite nanowire laser arrays. *ACS Nano* **2017**, *11*, 5766–5773. [[CrossRef](#)]
10. Frost, J.M.; Butler, K.T.; Brivio, F.; Hendon, C.H.; Van Schilfgaarde, M.; Walsh, A. Atomistic origins of high-performance in hybrid halide perovskite solar cells. *Nano Lett.* **2014**, *14*, 2584–2590. [[CrossRef](#)]
11. Szostak, R.; Silva, J.C.; Turren-Cruz, S.-H.; Soares, M.M.; Freitas, R.O.; Hagfeldt, A.; Tolentino, H.C.N.; Nogueira, A.F. Nanoscale mapping of chemical composition in organic-inorganic hybrid perovskite films. *Sci. Adv.* **2019**, *5*, eaaw6619. [[CrossRef](#)]
12. Lee, Y.M.; Yun, J.-H.; Matsuyama, A.; Kobori, S.; Maeng, I.; Lyu, M.; Wang, S.; Wang, L.; Jung, M.; Nakamura, M. Significant THz-wave absorption property in mixed  $\delta$ - and  $\alpha$ -FAPbI<sub>3</sub> hybrid perovskite flexible thin film formed by sequential vacuum evaporation. *Appl. Phys. Express* **2019**, *12*, 051003. [[CrossRef](#)]
13. Maeng, I.; Lee, Y.M.; Park, J.; Raga, S.R.; Kang, C.; Kee, C.-S.; Yu, B.D.; Hong, S.; Ono, L.K.; Qi, Y.; et al. Significant THz absorption in CH<sub>3</sub>NH<sub>2</sub> molecular defect-incorporated organic-inorganic hybrid perovskite thin film. *Sci. Rep.* **2019**, *9*, 5811. [[CrossRef](#)] [[PubMed](#)]
14. Lee, Y.M.; Maeng, I.; Park, J.; Song, M.; Yun, J.-H.; Jung, M.; Nakamura, M. Comprehensive understanding and controlling the defect structures: An effective approach for organic-inorganic hybrid perovskite-based solar-cell application. *Front. Energy Res.* **2018**, *6*, 6. [[CrossRef](#)]
15. Zhao, G.; Schouten, R.N.; Van Der Valk, N.; Wenckebach, W.T.; Planken, P.C.M. Design and performance of a THz emission and detection setup based on a semi-insulating GaAs emitter. *Rev. Sci. Instruments* **2002**, *73*, 1715–1719. [[CrossRef](#)]
16. Nagai, M.; Tanaka, K.; Ohtake, H.; Bessho, T.; Sugiura, T.; Hirosumi, T.; Yoshida, M. Generation and detection of terahertz radiation by electro-optical process in GaAs using 1.56  $\mu$ m fiber laser pulses. *Appl. Phys. Lett.* **2004**, *85*, 3974–3976. [[CrossRef](#)]

17. Ono, L.K.; Qi, Y. Surface and interface aspects of organometal halide perovskite materials and solar cells. *J. Phys. Chem. Lett.* **2016**, *7*, 4764–4794. [[CrossRef](#)] [[PubMed](#)]
18. Zhao, X.; Park, N.-G. Stability issues on perovskite solar cells. *Photon* **2015**, *2*, 1139–1151. [[CrossRef](#)]
19. Berhe, T.A.; Su, W.-N.; Chen, C.-H.; Pan, C.-J.; Cheng, J.-H.; Chen, H.-M.; Tsai, M.-C.; Chen, L.-Y.; Dubale, A.A.; Hwang, B.J. Organometal halide perovskite solar cells: Degradation and stability. *Energy Environ. Sci.* **2016**, *9*, 323–356. [[CrossRef](#)]
20. Jung, M.; Raga, S.R.; Qi, Y. Properties and solar cell applications of Pb-free perovskite films formed by vapor deposition. *RSC Adv.* **2016**, *6*, 2819–2825. [[CrossRef](#)]
21. Jung, M.; Kobori, S.; Matsuyama, A.; Maeng, I.; Lee, Y.M.; Kojima, H.; Bente, H.; Nakamura, M. Formation of CH<sub>3</sub>NH<sub>2</sub>-incorporated intermediate state in CH<sub>3</sub>NH<sub>3</sub>PbI<sub>3</sub> hybrid perovskite thin film formed by sequential vacuum evaporation. *Appl. Phys. Express* **2018**, *12*, 015501. [[CrossRef](#)]
22. Wagner, C.D.; Riggs, W.M.; Davis, L.E.; Moulder, J.F.; Muilenberg, G.E. *Handbook of X-ray Photoelectron Spectroscopy: A Reference Book of Standard Data for Use in X-Ray Photoelectron Spectroscopy*; Chastain, J., Ed.; Physical Electronics Division, Perkin-Elmer Corporation: Eden Prairie, MN, USA, 1995.
23. Tinkham, M. Energy gap interpretation of experiments on infrared transmission through superconducting films. *Phys. Rev.* **1956**, *104*, 845–846. [[CrossRef](#)]
24. Doniach, S.; Sunjic, M. Many-electron singularity in X-ray photoemission and X-ray line spectra from metals. *J. Phys. C: Solid State Phys.* **1970**, *3*, 285–291. [[CrossRef](#)]
25. Shirley, D.A. High-resolution X-ray photoemission spectrum of the valence bands of gold. *Phys. Rev. B* **1972**, *5*, 4709–4714. [[CrossRef](#)]
26. La-O-Vorakiat, C.; Xia, H.; Kadro, J.; Salim, T.; Zhao, D.; Ahmed, T.; Lam, Y.M.; Zhu, J.X.; Marcus, R.A.; Michel-Beyerle, M.E.; et al. Phonon mode transformation across the orthorhombic-tetragonal phase transition in a lead iodide perovskite {CH<sub>3</sub>}<sub>3</sub>NH<sub>3</sub>PbI<sub>3</sub>: A terahertz time-domain spectroscopy approach. *J. Phys. Chem. Lett.* **2016**, *7*, 1–6. [[CrossRef](#)]



© 2020 by the authors. Licensee MDPI, Basel, Switzerland. This article is an open access article distributed under the terms and conditions of the Creative Commons Attribution (CC BY) license (<http://creativecommons.org/licenses/by/4.0/>).